Thermo-fluid dynamic modeling of a supercritical carbon dioxide compressor for waste heat recovery applications

Giacomo Persico [a,*], Alessandro Romei [a], Paolo Gaetani [a], Ernani Fulvio Bellobuono [b], Lorenzo Toni [b], Roberto Valente [b]

[a] *Energy Department Politecnico di Milano, Milan, Italy*
[b] *Centrifugal Compressors and Expanders NPD Baker-Hughes Nuovo Pignone, Florence, Italy*

ARTICLE INFO

Handling Editor: Soteris Kalogirou

ABSTRACT

The development of novel technical solutions for the efficient recovery of waste heat is crucial for making accessible the large amount of thermal energy released by industrial processes, thus supporting the EU energy strategy. To this end, the EU-H2020 project CO2OLHEAT aims at developing and demonstrating a novel sCO_2 power unit of 2 MW capacity, recovering energy from flue gases at 400 °C. The CO2OLHEAT system features a relatively unconventional multi-shaft configuration where the sCO_2 compressor is driven by a dedicated radial expander, while the electrical power is generated via a separated axial turbine.

The present study focuses on the design and fluid-dynamic analysis of the CO2OLHEAT compressor. The thermodynamic optimization of the cycle led to an overall pressure ratio slightly above 2.5, delivered with a two-stage centrifugal compressor. As typically found in sCO_2 power systems, the thermodynamic state of the fluid at the machine intake (P = 85 bar; T = 32 °C) is close to the critical point and to the saturation curve; therefore, the first stage of the machine demands a dedicated aero-thermodynamic design, which can account for the effects of non-ideal thermodynamics and of the potential onset of two-phase flows. The paper discusses the conceptual aero-mechanical design of the compressor and then focuses on its performance assessment over the full operating range via Computational Fluid Dynamics. Two alternative CFD models are applied, the first one based on the barotropic fluid representation and the second one featuring a complete thermodynamic model, both of them assuming homogeneous equilibrium in presence of multi-phase flows. The experimental validation and the application of the two models are presented and discussed. They are shown to provide similar outcomes, and indicate that the compressor fulfills the system requirement and guarantees wide rangeability. A thorough comparison between the CFD results highlights the implications of the underlying physical differences between the models, thus allowing to properly evaluate their use for the aerodynamic design and analysis of sCO2 compressors.

1. Introduction

Energy-intensive industries across Europe release into the environment a large amount of hot flue gases, resulting in an enormous waste of heat that could, instead, be efficiently converted into useful mechanical or electrical energy. Considering the recent statistics on waste heat not exploited [1], an average conversion efficiency of 25%, and an operating factor of 0.8, the conversion of 5% of the European waste heat would lead to more than 500 GWh of primary energy savings per year.

While for flue gas temperatures below 300 °C and above 500 °C mature energy conversion technologies are available (Organic and

Steam Rankine Cycles, respectively), such technologies exhibit techno-economical limitations for flue gas temperature within this range. For such conditions, which represent a large share of the overall available waste heat in Europe, alternative technologies are presently under study. Among them, closed Joule-Brayton thermodynamic cycles working with carbon dioxide in supercritical conditions (sCO_2) are particularly attractive due to the high efficiency of the system and the compactness of their components, which might foster fast response to transients and reduced footprint, which are crucial features for effective waste-heat recovery systems [2].

Even though advanced calculations were performed at both

* Corresponding author.
E-mail address: giacomo.persico@polimi.it (G. Persico).

component ([3–9]) and system ([10–12]) level, and the first experimental verification of components gave promising outcomes ([13,14]), a proper demonstration of the overall system operation in the real environment is still needed. To this end, the EU-H2020 project CO2OLHEAT was launched in 2021, with the aim of developing a novel sCO$_2$ power system demonstration plant of 2-MW capacity, to be installed and operated in a real industrial environment, recovering waste heat from flue gases released at about 400 °C. By considering the flue gas conditions, as well as the required flexibility of operation, a simple recuperative sCO$_2$ cycle has been selected for the CO2OLHEAT system, with the sCO$_2$ compressor powered by a radial turboexpander and a subsequent axial turbine for electrical power generation.

The present study focuses on the design and the computational assessment of the sCO$_2$ compressor for the CO2OLHEAT power system. The thermodynamic optimization of the cycle led to an overall pressure ratio of 2.55, delivered by a two-stage centrifugal compressor. As typically found in such systems, at the machine intake the thermodynamic state of the fluid is close to the critical point and to the saturation curve (P = 85 bar; T = 32 °C); therefore, the first stage of the machine demands a proper aero-thermodynamic design, which must be capable to account for both the non-ideal thermodynamics of the fluid and the potential onset of phase change.

The design of the compressor was approached by leveraging the computational and modeling techniques developed in previous studies [9] and on the experimental survey recently carried out on a 5.4 MW sCO$_2$ prototype compressor [14,15]. At first, a conceptual design of the meridional channel and of the blade was carried out, then the compressor aerodynamics was verified by applying Computational Fluid Dynamics (CFD) over the entire flow range of the machine. Two thermodynamic models of the fluid were considered: at first, the experimentally validated barotropic model was considered [16], which allows representing in a simplified way the non-ideal thermodynamics of the fluid and the onset of two-phase flows, assuming homogeneous equilibrium between the phases; then, to enhance the reliability of the prediction, the compressor was also analyzed by applying a 'complete' homogeneous equilibrium model, which does not require the barotropic fluid assumption [17] and retains the actual thermodynamic complexity of the near-critical fluid.

The paper is structured as follows: first, the CO2OLHEAT system is presented and key indications on the compressor design are given; then the compressor aerodynamics and performance are analyzed with the two computational models, to derive conclusions on the machine operation and its modeling.

2. The CO2OLHEAT power unit

The CO2OLHEAT power unit was conceived to recover waste heat from an existing cement plant, whose flue gases in nominal conditions are available at a temperature of 400 °C and with a flow rate of 230000 Nm^3/h. The core of the system is a simple recuperated cycle without either recompression or recuperator bypass, due to the relatively low maximum temperature of the heat source and the high minimum stack temperature in order to avoid acid condenses (150 °C). As reported in Fig. 1, in the overall system the power unit is complemented by a waste-heat recovery unit and by a water-based heat-rejection unit.

The thermodynamic optimization of the sCO$_2$ cycle led to setting the compressor-intake thermodynamic conditions to 32 °C and 85 bar, to properly exploit the high density of CO$_2$ in the proximity of the critical point. The compressor-outlet pressure is set to 216.9 bar, resulting from a trade-off between cycle performance, material selection, and cost. The resulting cycle pressure ratio is, hence, equal to 2.55, which is obtained by two centrifugal compressors in series; they are mechanically driven by two centripetal turbines in series, thus creating a compact turbo-expander unit. The maximum temperature of the cycle is set at 360 °C, namely 40 °C lower than the flue gas nominal temperature in order to limit the surface area of the primary heat exchanger. The
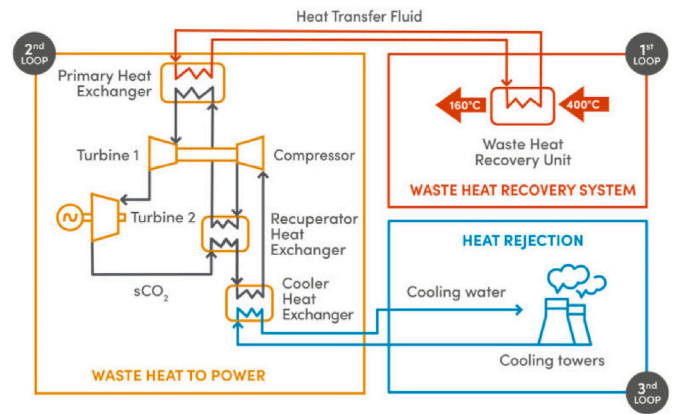

Fig. 1. Conceptual layout of the CO2OLHEAT system.

expansion is completed by an axial turbine, which is responsible for the power output of the system.

The resulting net power output exceeds 2 MW, with a cycle efficiency of about 23% referred to the inlet thermal power. Full details on the CO2OLEAT power system design and off-design operation can be found in Ref. [18].

3. Compressor design

The optimization of selected thermodynamic cycle requires the compressor to operate with a total pressure comprised between 85 and 216.9 bar, with inlet conditions (total temperature of 32 °C, density of 670 kg/m3) very close to CO$_2$ critical point.

The CO2OLHEAT turboexpander, shown in Fig. 2, is an integrally geared expander-compressor with an overall footprint of 2 × 1.9 m^2, for a total weight of 10 tons approximately, that combines a hot expander and a compressor. Gearbox (GB) has one low speed shaft (LSS) running at 3000 rpm and two high speed shafts (HSS), one dedicated to the compression section and one to the expansion phase; the LSS is connected to an electric motor used to start-up the machine and to control the speed to guarantee a steady-state operation of the integrated machine. The expander stages are installed on the first HSS, driving the compressor stages installed on the second HSS. The integrally geared configuration guarantees, moreover, the minimization of internal leakages impact and a proper management of the residual axial thrust.

The compression phase is made by two stages installed in back-to-back configuration on the shaft, as reported in Fig. 3. The first compression phase is equipped with a movable axial inlet guide vane (IGV) to guarantee a fine-tuning of the suction operating condition, and
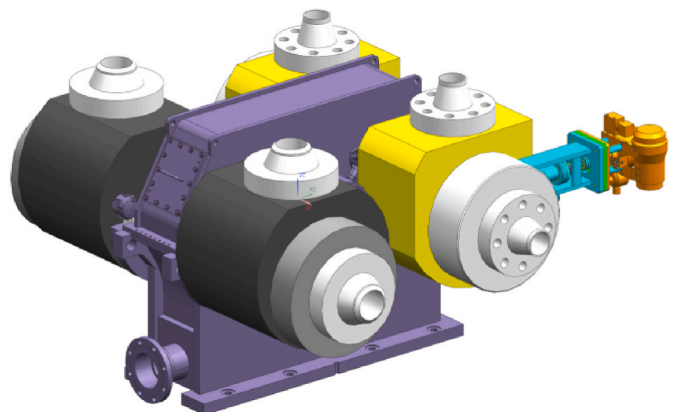

Fig. 2. Turbo-expander compact system © 2023 Baker Hughes Company - All rights reserved.
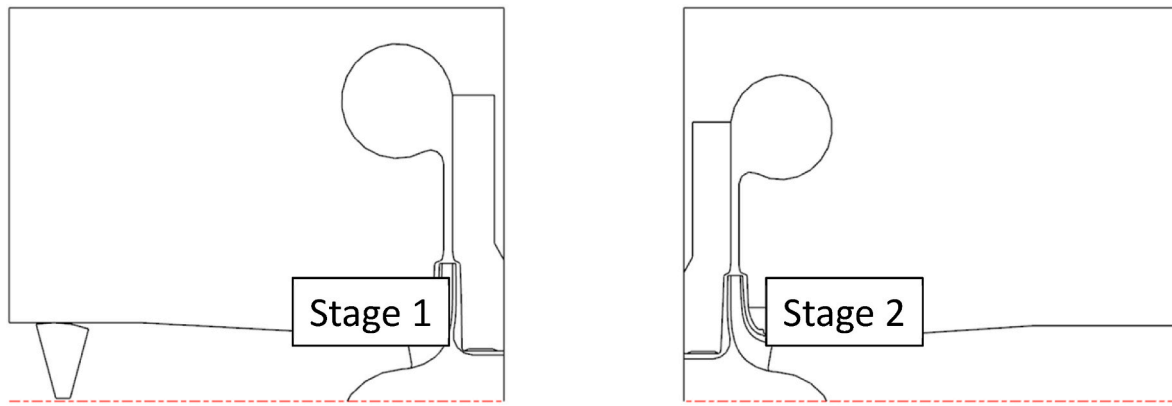
to improve compressor flexibility in off-design conditions. Due to the process conditions, a compact machine size was selected featuring shrouded impellers with external diameter close to 150 mm and an angular speed close to 20000 rpm. Based on the process inlet volume flow, the angular speed was selected as a result of a compromise between the aim of having an impeller flow coefficient in the recommended high-efficiency range and the need to keep the impeller size sufficiently large to guarantee manufacturability within good tolerances.

The CO_2 thermodynamic conditions at the inlet flange are slightly supercritical, with a small margin with respect to the saturation lines, both in terms of temperature and pressure, in particular for the first impeller. Moreover, the unavoidable pressure drop which occurs from the inlet flange to the first impeller suction section further decreases this margin.

For these reasons, phase change could occur in suction regions inside the machine, around the IGV blades and inside the first impeller. Specifically, the suction side of the blade, in the proximity of the leading edge, typically shows the lowest static pressure level and, potentially, a two-phase flow could onset within the rotor channel. When phase change occurs, thermodynamic quantities suddenly change and strong variations can arise for speed of sound (that may even halve), density, and specific heat: these aspects must be properly estimated, modeled, and and taken into accountin the impeller design process. Fig. 4 shows the sudden change in local speed of sound and compressibility which occurs when fluid conditions enter into the two-phase region, following an isentropic transformation.
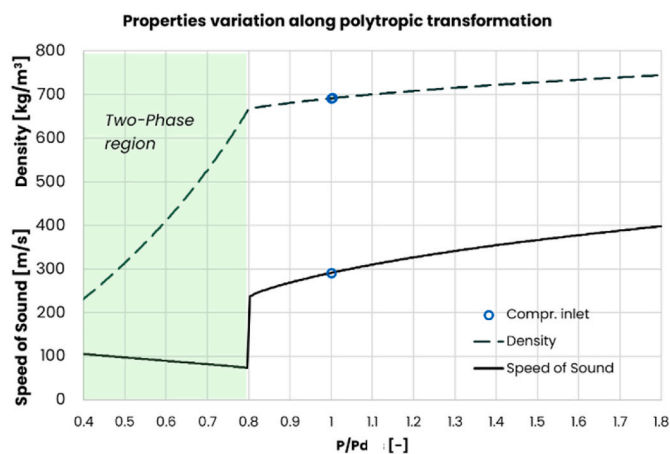
As described in the following paragraph, the design of this machine requires an approach leveraged on tailored numerical modeling, able to deal with both strong non-ideal gas behavior and the effect of potential phase change.

The first impeller, whose flow coefficient (defined as $\varphi = 4Q_0/(\pi D_2^2 u_2)$) is 0.0320, therefore featured a dedicated design to cope with the near-critical CO_2 characteristics and focused to mitigate the impact of possible phase change during operation: a proper optimization was needed when defining the streamwise evolution of the cross section of the flow path, and the intake region was designed to minimize the acceleration and the risk of cavitation. To this end, in the stage conceptual design, the following features have been selected: at first, an impeller equipped with splitter blades to decrease the blockage at the inlet and mitigate the risk of anticipated chocking; secondly, an appropriate definition of the impeller cross-section to take into account the low compressibility of sCO2. Attention was paid to blade loading as it was optimized to locally avoid or mitigate the pressure drops towards saturation line. A three-dimensional view of the first stage impeller is depicted in Fig. 5.

4. Numerical methods

The computational flow models applied in this study are based on the Ansys Fluent finite-volume solver. In this work, we compare two alternative formulations to deal with non-ideal compressible two-phase flows
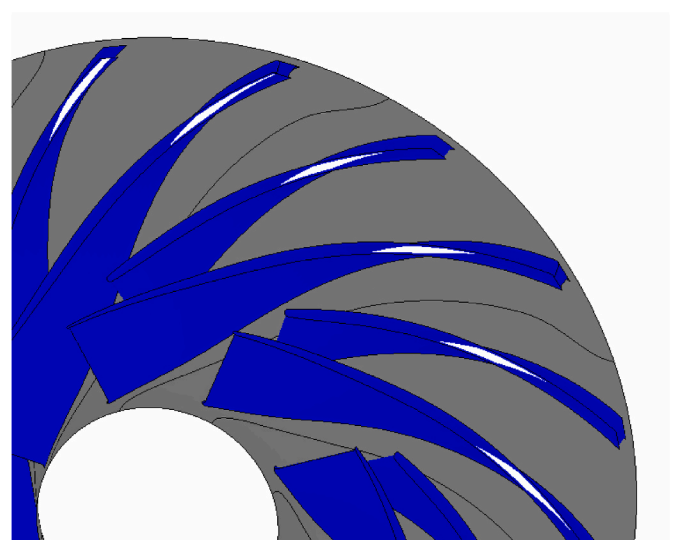

Fig. 4. Abrupt change in speed of sound and compressibility where fluid conditions cross saturation line, along an isentropic transformation.

Fig. 5. Three-Dimensional View of the Impeller Geometry

of CO_2, named *homogeneous equilibrium model* (HEM) and *barotropic model*, respectively. Both models describe the two-phase flow as a homogeneous mixture, hence single-phase governing equations are recovered and expressed in terms of average properties. The turbulence effects are introduced with the $k - \omega$ SST model [19], adding a rotation-curvature correction to the production terms of k and ω [20]. Whenever walls are modeled as smooth, the turbulence equations are resolved at the wall having wall-adjacent cells in the viscous sublayer (i.e., $y^+ < 3$). Otherwise, wall functions are employed to account for roughness effects. In the following, the details of the thermodynamic models, the numerical schemes, and the calculation set-ups are reported, followed by the experimental validation of the computational framework.

4.1. Thermodynamic models

The HEM features an enthalpy-based energy equation in place of the standard energy equation based on the total enthalpy. This replacement is essential to address the specific requirement imposed by Ansys-Fluent, which mandates the use of temperature as a state variable when incorporating non-ideal equations of state. Following this modification, pressure and specific enthalpy can be used as independent state variables, straightforwardly recovering thermodynamic equilibrium properties for the two-phase mixture consistently with the Span-Wagner equation of state. The complete flow model and its implementation are reported in Ref. [17].

To speed up the calculation, a look-up-table (LUT) approach is implemented to call thermodynamic properties within flow solver iterations. The LUT boundaries are set to avoid extrapolated values in the solution, and they are $P \in [20, 300]$ *bar* and $h \in [151, 588]$ *kJ/ kg*, with $h_{ref} = 200 \ kJ/kg$ at $T = 273.15 \ K$ and saturated liquid condition. 1201×1201 grid points are identified by uniform steps in pressure (0.233 bar) and specific enthalpy (0.364 kJ/kg). The appropriateness of the LUT discretization is discussed in Ref. [17].

On top of the HEM assumptions, the barotropic model introduces a simplification in the thermodynamic treatment. Thermodynamic and transport properties are assumed to depend only on the local pressure, hence neglecting the thermal and volumetric effects due to loss generation (the fluid is then considered compressible but not thermally expandable). Such an assumption simplifies the flow modeling with respect to the full HEM, but it provides crucial advantages from the computational perspective. The barotropic model completely decouples mechanical from thermal effects, removing the need of solving the energy equation to determine the flow field. Moreover, the solver becomes inherently more robust than the one based on the full model in particular for supercritical fluids, because the solution does not need to handle the specific heat at constant pressure, which exhibits sharp gradients close to the critical point (wherein it becomes singular). These features make the barotropic model computationally efficient and inherently suitable for tackling the numerical simulation of two-phase flows in sCO_2 compressors. To determine the barotropic thermo-physical relationships (for density, viscosity, speed of sound), a choice on the entropy generation across the polytropic process across the machine has to be made. In this study, an isentropic law (considering the entropy of the inlet state, s = s_d) was assigned for calulating the barotropic relations. It is to be noted that building the barotropic relationships based on the upstream entropy does not imply to compute an isentropic flow, as the mechanical dissipation is properly introduced into the model by viscous and turbulent terms in the momentum equation; the barotropic assumption only neglects the thermal correction to the thermo-physical properties (the density, in particular) due to the dissipation. Full details on the barotropic flow model and its implementations are reported in Refs. [9,16].

In this study, the barotropic relations are implemented in the solver via a LUT approach: thermo-physical properties are tabulated as a function of pressure at the entropy of the intake thermodynamic state, using for pressure the same boundaries and discretization step reported for the HEM.

4.2. Numerical schemes

The system of equations (continuity, momentum balance, turbulence model, and, if needed, energy balance) is solved in the following way: continuity and momentum balance are solved in a coupled fashion, then the two turbulence equations and, if needed, the enthalpy-based energy equation. After this step, thermo-physical properties are updated, and the procedure is iterated until achieving numerical and physical convergence. Advective terms of continuity, momentum, and enthalpy-based energy equation are discretized with the QUICK scheme. A cell-to-cell flux limiter is applied to reduce spurious oscillations near discontinuities. Advective terms of turbulence equations are discretized with a linear upwind scheme. All diffusive terms are discretized with a second-order central differencing scheme. The gradients are computed with the least squares cell-based method. A second-order accurate method is selected to interpolate the pressure from cell centers to cell faces.

4.3. Calculation set-up

The computational grid for the calculations presented in this paper is composed of hexahedral elements and was generated with AutoGrid™. The computational domain includes the main and splitter blade, with fillet radii, and the vaneless diffuser. A single-blade passage is modeled, by exploiting periodic boundary conditions. As the aim is to investigate the internal flow aerodynamics, the inlet guide vanes as well as the leaks in the seals and the related secondary flows are not modeled in the CFD simulation. After a preliminary grid-dependence analysis, a mesh composed of about 3 million cells was selected.

Calculations were performed by assigning the total state at the inlet section. The flow rate was imposed at the outflow, except close to choked-flow conditions, for which an average static pressure was assigned at the outlet. No-slip boundary conditions were imposed on the solid walls. As the flow domain is rotating with the impeller, a counter-rotating velocity was assigned at the endwalls of the vaneless diffuser.

4.4. Experimental validation

The two computational models presented in Section 3.2 were validated against experiments performed on the MW-scale sCO_2 compressor designed, manufactured, and tested in the frame of the EU project sCO2-Flex. The sCO2-Flex test campaign is a relevant reference for the validation of sCO2 compressor prediction tools: (i) the prototype machine capacity (5 MW) is representative of industrial applications; (ii) the design was tailored for near-critical operation; (iii) the compressor was run in nominal conditions, in terms of both peripheral Mach number and thermodynamic state; (iv) several tests were also carried out for different thermodynamics conditions at the intake, so to cover a wide range of off-design operating condition in which the machine may work. Full details on the test set-up, the instrumentation, and measurement uncertainty are reported in Ref. [14]; the same publication also reports a comparison between the measured pressure ratios and the one predicted by CFD simulations performed with a barotropic thermodynamic model, fully consistent with the one used in the present paper. The characteristic curves of the compressor were obtained and compared for four intake conditions, all of them close to the critical point, so to cover a wide range of fluid behaviours, from liquid-like ($T_{T,in}$ = 304.15 K; $P_{T,in}$ = 79.79 bar) to vapor-like ($T_{T,in}$ = 309.15 K; $P_{T,in}$ = 79.79 bar), and even in pseudocritical conditions ($T_{T,in}$ = 307.65 K; $P_{T,in}$ = 79.79 bar). The good agreement between the experiments and the barotropic CFD simulation validated the assumptions of homogenous equilibrium and barotropic thermodynamics.

In this paper, we enrich this CFD validation study by adding the comparison with the HEM CFD solver. This allows to verify and

experimentally validate this latter model and to provide a first comparison between the two CFD models used in this paper. The new HEM calculations were performed using the models and schemes described in sections 3.2 and 3.3, considering wall roughness, and using a mesh composed of about 3 million elements, which guarantees mesh-independence of the results. Fig. 6 shows the compressor curves, in terms of pressure ratio as a function of the flow coefficient, derived from the experiments and the two CFD models, for all four thermodynamic states.

The four trends reported in Fig. 6 indicate two main effects of the intake states: (i) the pressure ratio delivered by the machine changes significantly, being progressively higher as the intake temperature reduces (i.e., when passing from vapor-like to liquid-like behavior); (ii) the right limit of the machine changes significantly, and it does not follow the expected dependence on the peripheral Mach number. These effects can be explained by resorting to the non-ideal thermodynamics and the onset of two-phase flows, resulting from the operation of carbon dioxide close to the critical point [14].

The agreement between the experimental and computational results is very good in terms of curve shapes and operating range, in all the conditions; in particular, the two main effects observed above are perfectly captured by both the CFD models, and the measured choking flow rate is matched within 3% by both the computational models. In fact, the CFD models slightly overestimate the pressure ratio with respect to the experimental data; however, this is expected, since in the CFD simulations the leakage flows into the eye seal are not modeled.

This experimental assessment confirms the reliability of the homogeneous equilibrium assumption for the prediction of the two-phase flow in sCO_2 compressors. This allows to consider the two models used in the present work, both of them based on this assumption, capable of reliably predicting the operation and the rangeability of the CO2OLHEAT compressor. With respect to what was documented in Ref. [15], in this paper we introduce the comparison with the 'full' HEM simulation, thus eliminating the barotropic assumption. The two CFD predictions exhibit very marginal differences, in all the tested conditions. The comparison between the models is one of the cores of this paper and it will be discussed in detail in Section 5, focusing on the CO2OLHEAT compressor.

5. Compressor performance

The computational flow models described in the previous section were applied to investigate the aerodynamic performance of the first stage of the CO2OLHEAT compressor, namely the one most affected by the near-critical fluid state and which required a tailored design. Since the compressor was designed by resorting to a combination of preliminary codes and the CFD barotropic model, the predictions obtained with this model are used for a first assessment of the compressor performance. In this first analysis, conventional smooth walls are also considered. Fig. 7 reports two operational curves of the machine, related to the pressure ratio (left) and total-total efficiency (right) for the nominal angular speed and flow rate (corresponding to IGV in stagger position equal to 0°). The curves are scaled with respect to the values obtained for the nominal condition, for confidentiality reasons.

The curves cover a wide range of flow conditions, from 75% to 145% of the design flow rate. On the curves, the chocking limit (labelled as "C") and the left one (labelled as "L") are reported. The left limit was set *a priori*, since no expected plant operating condition should require flow coefficients below that value (also in consideration of the availability of IGVs). However, it is important to remark that the simulations for the lowest flow rate condition did not exhibit any trace of computational instabilities which normally arise approaching aerodynamic stall, thus suggesting that the actual stall/surge limit of the machine may be below the 75% of the nominal flow coefficient. The left frame of Fig. 8 shows the distribution of relative Mach number in the midspan section for the lowest flow rate considered. The figure indicates a very low level of compressibility, as the relative Mach number remains below 0.3 in almost the whole flow surface; local accelerations appear on the suction side of the blades, as a consequence of the positive incidence, but no traces of separation appear, thus excluding any risk of blade stall.

The situation is completely different for the conditions close to the right limit (right frame of Fig. 8). The field clearly shows the onset of choking for a flow rate equal to 145% of the design one, verified by running multiple CFD simulations for different pressure ratios. Even though occurring at high flow rate, the choking is anticipated with respect to the value expected by neglecting the onset two-phase flows; this phenomenon was clearly shown in a previous study, where a CO_2 compressor was operated in conditions near and far from the critical point [21]. The right frame of Fig. 8, showing the Mach number distribution at midspan for the right limit condition, shows that upstream of the blades the Mach number remains below 0.5; however, as the flow enters within the bladed channel, the combination of blade thickness, blade aerodynamics, and negative incidence promotes a static pressure drop sufficiently large to trigger phase change; this, in turn, implies an abrupt rise of relative Mach number, causing the onset of choking due to the abrupt drop of speed of sound in the two-phase region [22]. The value of the chocking flow rate, which in principle depends on the degree of chemical and thermal equilibrium established between the phases of the mixture, was found to be properly captured by models based on the homogeneous equilibrium assumption, such as the present barotropic one, by virtue of the experimental validation study first documented in Ref. [14] and here recalled in Section 3.4.

In light of the present analysis, the first CO2OLHEAT compressor is capable of providing the expected performance in a very large range of operations, confining the most severe effects of two-phase flows to very high flow rate conditions, not expected in the off-design operation of the system.
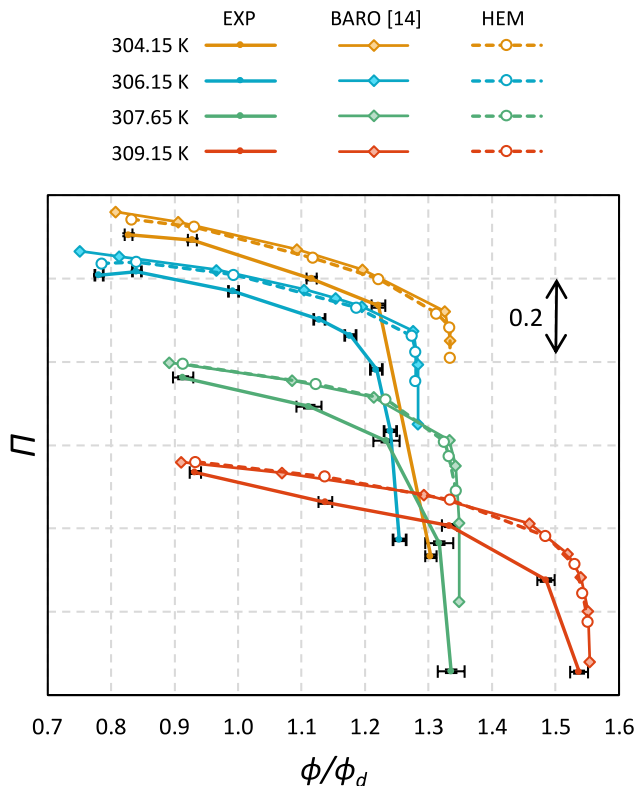

	EXP	BARO [14]	HEM
304.15 K			
306.15 K			
307.65 K			
309.15 K			

Fig. 6. Compressor curves (pressure ratio – flow coefficient) for multiple inlet thermodynamic states (please note that extension of each vertical division in the ordinate is 0.2). © 2023 Baker Hughes Company - All rights reserved.
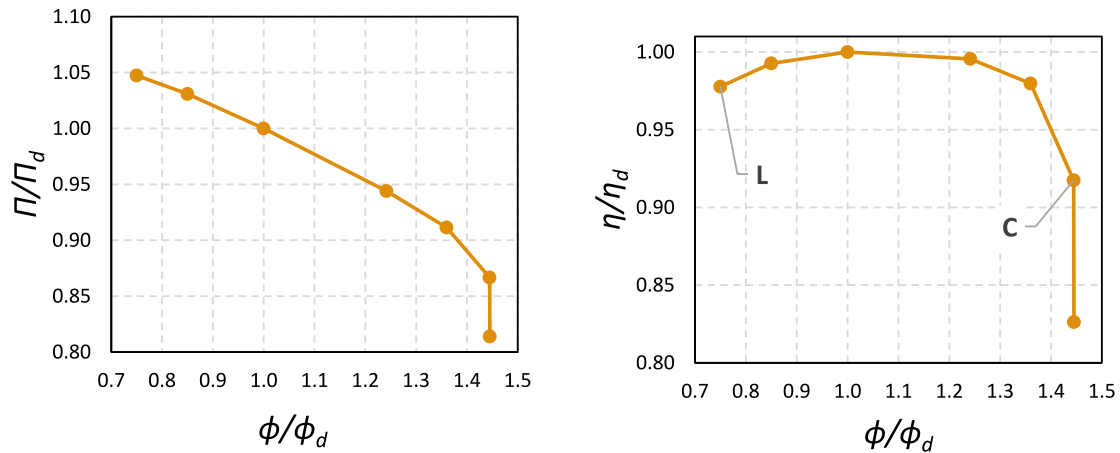
Fig. 7. Operational curves of the first stage of the compressor simulated with the barotropic model and smooth walls. Left: pressure ratio; right: total-total efficiency. © 2023 Baker Hughes Company - All rights reserved.
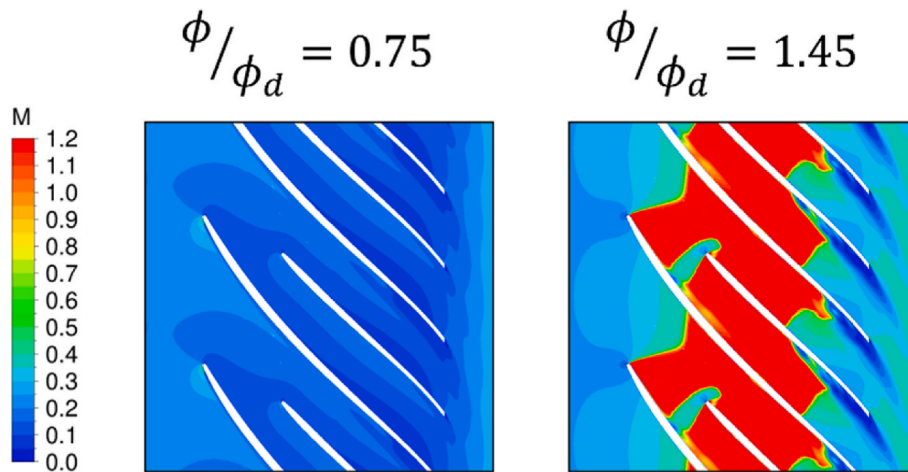

Fig. 8. Mach number distributions at midspan for 75% (left) and 145% (right) of the nominal flow rate. © 2023 Baker Hughes Company - All rights reserved.

6. Model comparison

The CFD model based on the barotropic fluid assumption features a conceptually simple and computationally effective mathematical formulation. However, with the aim of improving the generality and reliability of sCO_2 compressor simulation tools, its verification against more complex models is crucial to evaluate its range of validity. In this work, the barotropic model is verified against simulations of the flow in the first CO2OLHEAT compressor performed with the HEM code, which still assumes equilibrium in the dynamics of two-phase mixtures, but removes the barotropic assumption. In this way, the thermal and volumetric effects of the entropy generation by dissipation across the compressor are taken into account; as a consequence of the volumetric effect, a correction on the meridional flow component might occur, with potential implications on compressor work exchange, pressure rise, and efficiency. It should be noted that, when constructing this 'higher-fidelity' simulation tool, we still focused on a homogeneous equilibrium of the two-phase flow that might occur in the machine. This is motivated by the experimental validations available in literature for flashing flows in sCO_2 nozzles [16], ejectors [23], and sCO_2 compressors [14], which all agree in recognizing a good capability of the HEM in reproducing the phase change processes evolving from supercritical or near-critical states. For this reason, it was deemed relevant, at this stage of the study of sCO_2 compressors, to remove the barotropic assumption rather than to consider non-equilibrium multi-phase models.

The comparison between the two models is discussed at three levels: at first, the compressor performance and rangeability are considered; then, the streamwise distributions of relevant quantities along the machine are discussed for three conditions, namely in the nominal one and close to the right and left limits; finally, the flow pattern on the blade-to-blade surface at midspan is discussed to highlight the model implications on detailed flow features.

6.1. Compressor performance

Fig. 9 shows the operational curves, in terms of pressure ratio and efficiency, as simulated by both the barotropic model and the HEM. The curves exhibit a noteworthy agreement, both qualitative and quantitative, suggesting that the thermal effects of losses play a negligible role in the compressor performance. Moreover, as already found in Section 3.4 for the sCO_2-Flex compressor, the two models predict exactly the same rangeability of the machine.

It is to be noted that the right limit is an outcome of the simulation and, as already observed, it is caused by the onset of two-phase flows, which leads to an abrupt rise of the Mach number in the intake region of the impeller. The fact that the two models predict the same limit indicates that the barotropic assumption does not alter the prediction of the onset of two-phase flow. In the following sections, more detailed
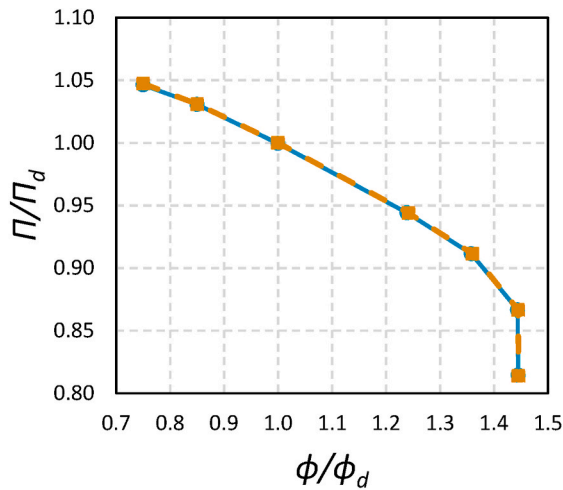
Fig. 9. Comparison between operational curves of the first stage of the compressor simulated with the barotropic model and the HEM, for smooth walls. © 2023 Baker Hughes Company - All rights reserved.

flow features are considered to explain this result, at first considering the flow evolution along the machine.

6.2. One-dimensional flow configuration in the streamwise direction

To investigate the flow evolution in the streamwise direction, Fig. 10 reports the distributions, along the meridional coordinate of the machine, of cross-section averages of density and meridional velocity in the nominal condition, for both the computational models. In this kind of plot, the leading edges of the main and splitter blades are placed at a streamwise coordinate of 0.23 and 0.31 respectively, while the trailing edges are placed at a streamwise coordinate of 0.62.

First considering the density trend, it exhibits a slight reduction upstream of the main-blade leading edge, followed by a regular increasing trend, which terminates with an overall density rise of about 10% of the intake value (this moderate increase in density indicates the low compressibility of the fluid in the nominal condition).

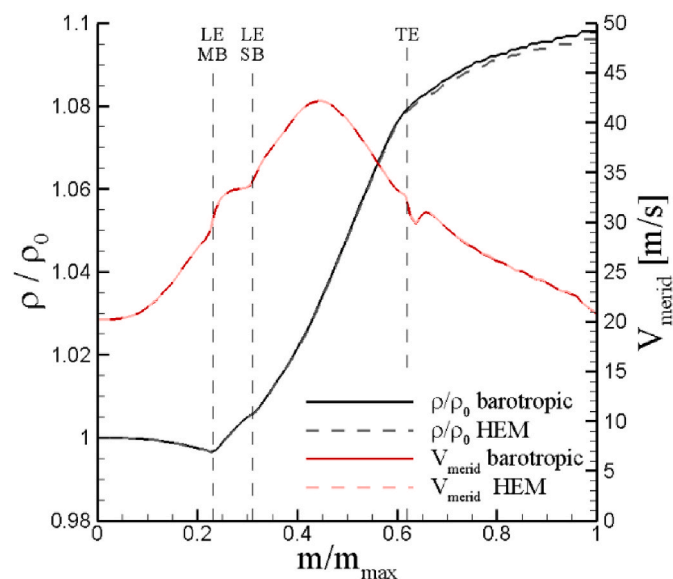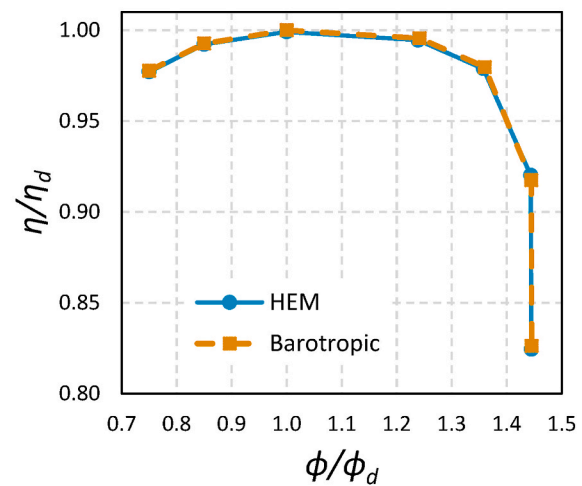As already remarked, the barotropic assumption does not include the

volumetric effect of dissipation, which heats and, hence, dilates the fluid as the entropy is generated along the (adiabatic) irreversible compression process. Fig. 10, indeed, shows a deviation between the barotropic and HEM predictions as the compression proceeds along the machine, with a lower density computed by the HEM. Such differences are completely negligible upstream and within the impeller (up to the trailing edge of the blades) while they become visible in the vaneless diffuser section, due to the dissipation generated by the blade wake and its mixing. The maximum difference, however, is of the order of 0.2% of the actual density value, or 2% of the (already small) change in density across the machine.

The change in density might have an impact on the flow configuration and in the velocity triangles, as it might alter the prediction of meridional velocity, defined as the vectorial sum of the axial and radial components. To shed light on the velocity field, Fig. 10 also reports the streamwise distribution of the meridional flow velocity for the barotropic and HEM predictions. The distributions show an increase in meridional velocity within the impeller, with local disturbances in correspondence to the leading and trailing edges of the blades. The diagram also indicates that the impact of the barotropic assumption is everywhere negligible since a 0.2% variation in the density estimate does not produce any significant alteration to the kinematics of the machine.

To extend the analysis to the whole compressor curve, Fig. 11 reports the same quantities as Fig. 10 for the left and right limit conditions of operation of the compressor identified in Fig. 7. The same considerations made for the nominal condition apply to the lowest flow rate condition, while a different flow configuration emerges at high flow rate, which is characterized by cavitation-induced choking. In this latter case, the density of the fluid undergoes a severe drop in the proximity of the main-blade leading edge and further reduces in correspondence to the leading edge of the splitter blade; the density finally reaches its minimum value in the central region of the channel, where the meridional velocity exhibits its peak value, and the two-phase mixture occupies the whole channel. Then, the density progressively rises and the fluid reverts to single phase in the rear part of the impeller (from ~0.52 streamwise coordinate onwards). In the central part of the channel, where the largest oscillations take place, the models exhibit slight local differences in density, which however disappear in the rear part of the impeller; as already observed in the other conditions, a residual marginal difference in density remains at the stage exit, of about 0.6% of the local density value, or 1.6% of the density variation along the impeller. In terms of meridional flow velocity, minor variations appear also in this case, even in the two-phase region in the center of the channel.

Fig. 10. Streamwise evolution of density and meridional flow velocity along the meridional coordinate in nominal condition (LE-MB: leading edge main blades, LE-SB: leading edge splitter blades; TE: blades trailing edge). © 2023 Baker Hughes Company - All rights reserved.
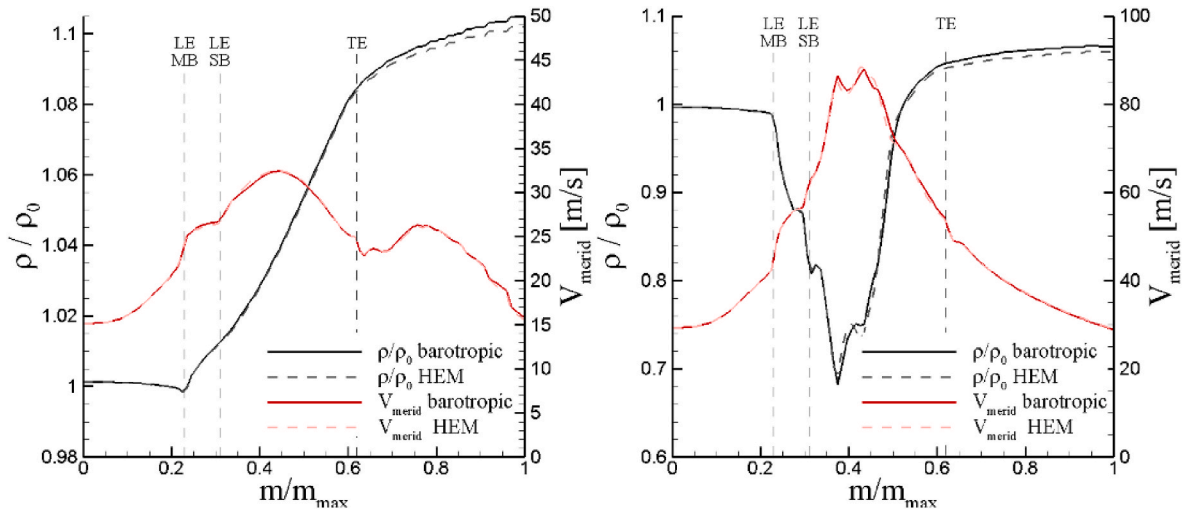
Fig. 11. Streamwise evolution of density and meridional flow velocity along the meridional coordinate for 75% (left) and 145% (right) of the nominal flow rate. © 2023 Baker Hughes Company - All rights reserved.

6.3. Flow morphology

The comparisons reported in Sections 5.1 and 5.2 have shown that the barotropic model is able to predict the gross features of the flow, in terms of overall performance and one-dimensional flow distribution. However, the complexity of the loss mechanisms occurring within the impeller suggests complementing the model comparison by considering the detailed flow morphology and searching for local effects of the barotropic assumption. To this end, Figs. 12 and 13 show the distributions of some relevant flow quantities on the blade-to-blade surface at midspan, as predicted by the two models, for the nominal and chocked-flow conditions respectively (the flow in the left limit condition was
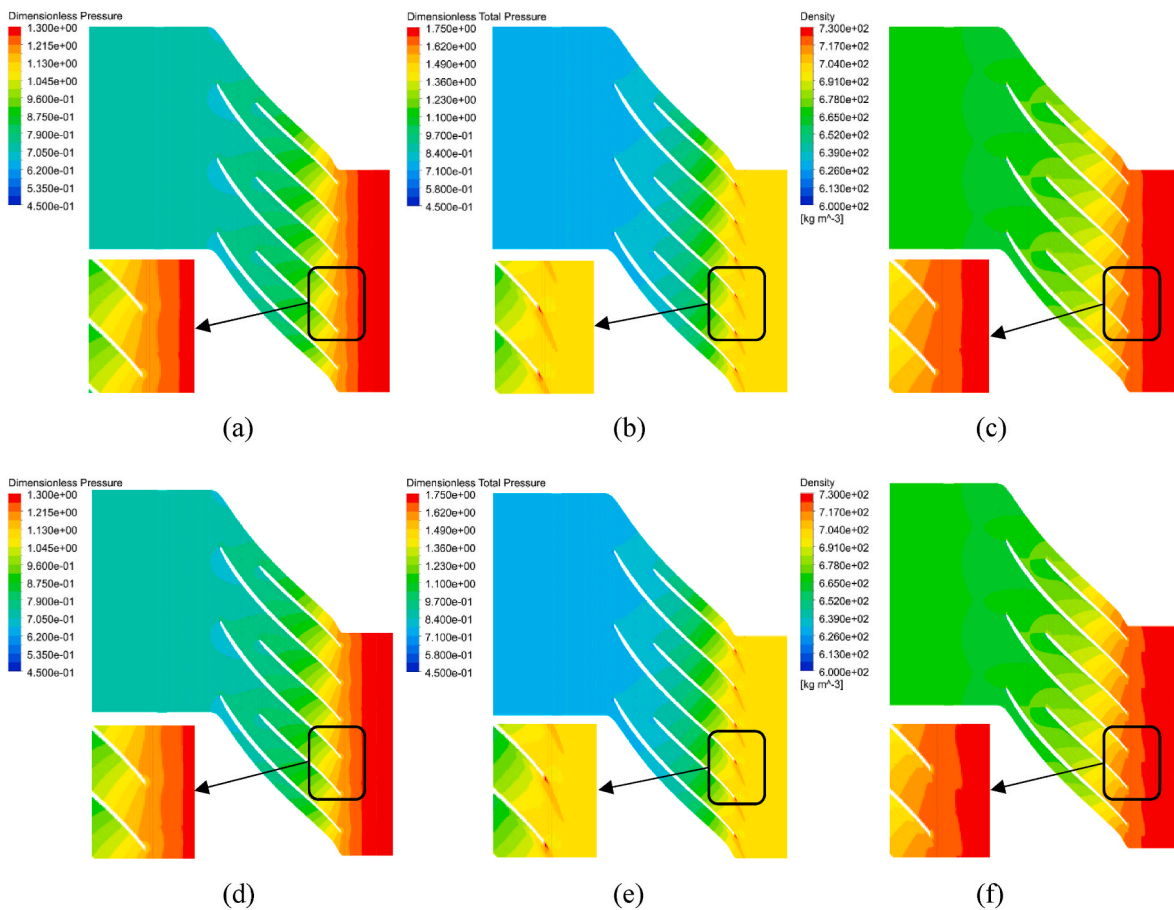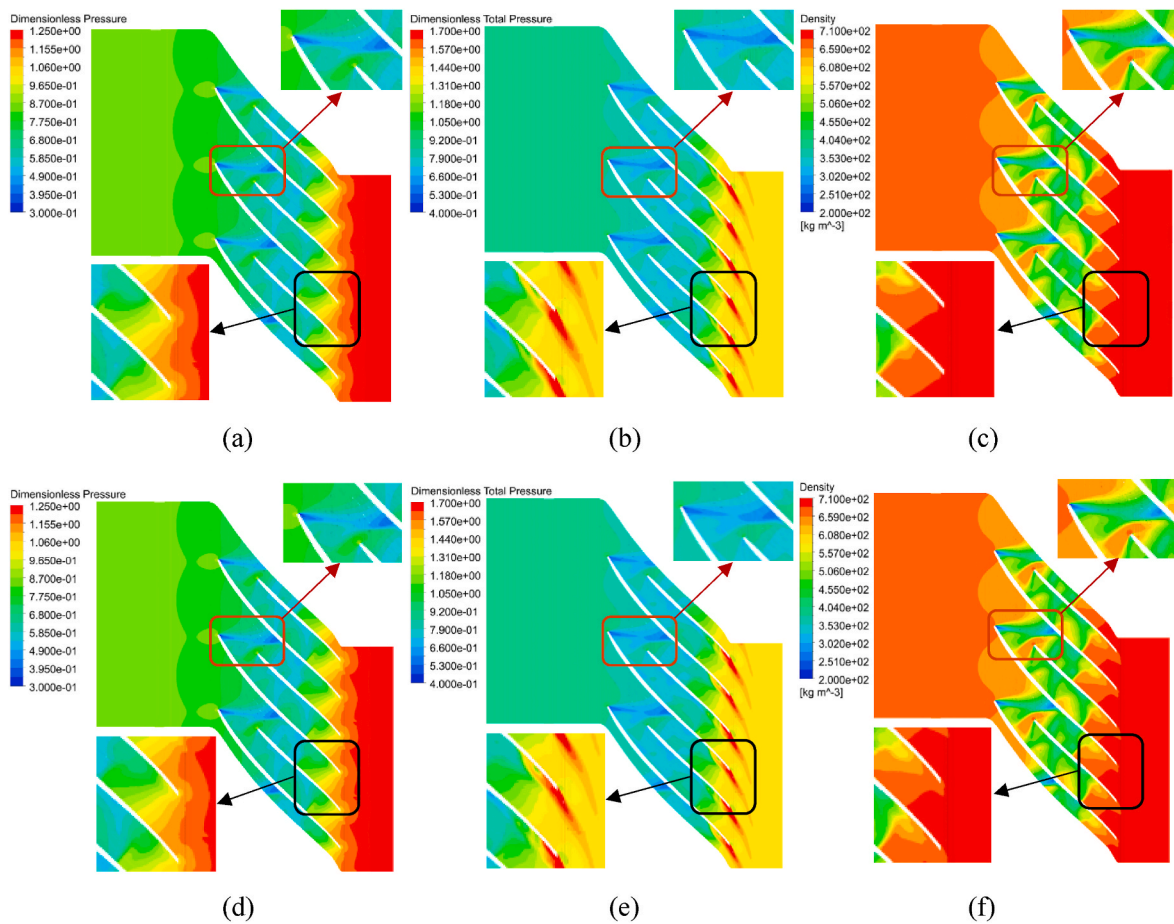

Fig. 12. Flow configuration at midspan for dimensionless pressure (a, d), dimensionless total pressure (b, e), and density (c, f) in nominal condition predicted by barotropic model (a, b, c) and HEM (d, e, f). Zooms of the fields contained in the boxes marked in the frames are reported for sake of clarity. © 2023 Baker Hughes Company - All rights reserved.

Fig. 13. Flow configuration at midspan for dimensionless pressure (a, d), dimensionless total pressure (b, e), and density (c, f) in choked-flow condition predicted by barotropic model (a, b, c) and HEM (d, e, f). Zooms of the fields contained in the boxes marked in the frames are reported for sake of clarity. © 2023 Baker Hughes Company - All rights reserved.

excluded for sake of brevity, due to its similarity with the one in nominal condition). In these plots, the static and total pressure values are made dimensionless with respect to corresponding averaged pressure values in the domain, for confidentiality reasons.

In the nominal condition (Fig. 12) any differences in the flow solutions are hardly visible. The pressure fields, reported in frame (a) and (d) show the suction in the front part of the blade and a smooth pressure rise along the machine. Just downstream of the trailing edge of the blades, a weak azimuthal pressure perturbation appears, quickly decaying in the vaneless diffuser. The (absolute) total pressure field, reported in frames (b) and (e), exhibits a smooth distribution in the leading edge regions of both the main and splitter blades, and a progressive growth along the channel. At the trailing edge of the blades, an interesting feature appears: the loss mechanisms occurring in the rear part of the channel (the growth of the boundary layer on the suction side of the blade and the shedding of the viscous wake from the blade trailing edge) introduce a significant azimuthal perturbation in the total pressure field, marked by the black rectangular boxes reported in all the frames. In these highly dissipative regions, low relative velocity is coupled with high peripheral speed, leading to high absolute velocity and, hence, high total pressure.

The barotropic model, which is capable of reproducing reliably both the pressure field and the kinematics of the fluid in the machine, reproduces these features in full agreement with the ones predicted by the HEM. However, local differences appear in the density fields, reported in frames (c) and (f), as a result of the loss mechanisms occurring within and downstream of the channel. Since very minor losses occur in the front part of the blade, in this region perfect agreement is found between the two models. In the rear section of the blade, where the rectangular

box is placed, the effects of losses on the density appears in the HEM prediction (frame f) in the form of an azimuthal perturbation on the suction side of the blade and, especially, in the region of the blade wake, producing a wavy density distribution downstream of the blade trailing edge: in these regions of the flow the dissipation increases the thermal energy of the fluid, which slightly dilates locally. This effect is, in fact, the unique flow feature that cannot be reproduced by the barotropic model, which indeed shows, in the same region, a regular increasing trend without azimuthal perturbations. It is to be noted that, as the wake is quickly mixed out downstream of the impeller, in the vaneless diffuser the two density fields quickly recover a uniform trend.

The flow configuration in the choked-flow condition, reported in Fig. 13, is much more complex than that in the nominal one, as already observed in Fig. 11. First considering the pressure and total pressure fields, we note a significant pressure drop as the flow enters within main-blade the channel, highlighted in the red rectangular boxes marked in all the frames. Here, as already observed in Fig. 8, the very low pressure zone covers the entire channel and triggers the onset of two-phase flows, the drop in speed of sound, and finally the choking. The pressure drop, mainly caused by the blade blockage, also alters the total pressure in a similar way. Within the channel, the pressure is modulated by the splitter potential field and blade thickness. In the rear section of the channel, highlighted by the black rectangular boxes reported in all the frames, high azimuthal pressure perturbations appear and a wide region of dissipation (i.e., low relative velocity) is marked by high total pressure values. This latter results from the severe losses caused by a separation in the rear suction side of the blade, which joins with the loss caused by the blade wake.

All these flow features are well captured by the barotropic model, which does not exhibit any relevant difference with respect to the HEM. Differences are expected in the density field, and visible in frames (c) and (f). However, despite the much higher flow complexity, the comparison between the barotropic and the HEM density fields does not show alternative features with respect to those already observed for the nominal condition. The correspondence between the two flow predictions in particular in the intake region where choking occurs explains the perfect matching between the two models in setting the right limit of the compressor.

Overall, the impact of losses on the density is visible in the HEM prediction mainly in the rear suction side of the blade, where minor – though visible – differences appear with respect to the barotropic simulation result.

It is to be noted that, in the presence of such a massive cavitation process, any model assuming homogeneous equilibrium necessarily reproduces a simplified flow field downstream of the two-phase sonic throat, with respect to the one resulting from a real phase-change process. However, for sCO_2 compressor applications, and the CO2OLHEAT one in particular, the cavitation-induced choking sets a theoretical limit where the machine should not be operated, not only because of performance drop but also because of structural integrity and erosion issues which might be triggered by such a massive cavitation. From this perspective, design tools must be primarily capable of predicting the onset of cavitation, rather than resolving the cavitating flow development downstream, which would probably need a more complex multiphase flow model.

7. Impact of wall roughness

The power capacity of waste heat recovery systems is relatively low with respect to conventional power systems, especially in the present demonstration plant. This feature, combined with the inherent compactness of sCO_2 machines, makes size effects particularly relevant for the CO2OLHEAT compressors. In an effort of investigating the aerodynamic impact of small size, a computational evaluation of the wall roughness was performed, using the complete HEM model and simulating the entire range of machine operation. An equivalent sand grain roughness k_s equal to 5 μm was selected, representative of standard manufacturing technology, though not indicative of the manufacturer's capabilities. Nonetheless, for this fluid in the thermodynamic conditions of interest, the thickness of the viscous sublayer is estimated to be of the order of 10^{-2} μm, thus one might expect that such a value of surface roughness will alter the development of the boundary layer and the associated loss generation.

Fig. 14 compares the curves of total-total pressure ratio and efficiency of the first stage of the CO2OLHEAT compressor showing important quantitative effects. In the nominal flow rate conditions, the roughness reduces by 1% the pressure ratio and by 3% the efficiency. These differences are maintained fairly constant along the whole operating range (the lower difference appearing at the choking is, in fact, an artificial effect of the nearly vertical shape of the curve in this region, which greatly complicates the comparison between different conditions). Moreover, the roughness does not influence the left limit, where, again, no traces of stall onset appeared in the simulations, and especially at choking, which is reached for the same flow rate found for the smooth-wall calculation.

These results confirm the significant quantitative role of wall roughness in terms of compressor performance, suggesting care in the selection of the manufacturing process, but they also indicate a limited impact of roughness on the compressor rangeability.

8. Conclusion

This paper has presented a computational study of the near-critical sCO_2 compressor of the CO2OLHEAT waste heat recovery system. The machine, composed of two back-to-back compressor stages, features an integrated architecture and a non-conventional design approach for the first impeller, due to the thermodynamic complexity associated with the working fluid, which is operated close to the thermodynamic critical point.

The thermo-fluid dynamics of the first stage of the compressor was analyzed with Computational Fluid Dynamics, applying two alternative fluid thermodynamic models: in the first solver, the fluid is assumed to follow a barotropic equation of state, while the second one features a 'complete' thermodynamic model. Both the solvers are capable of simulating non-ideal two-phase flows of sCO_2, under the assumption of homogeneous equilibrium between the phases. The two models were validated against experiments on a MW-scale sCO_2 compressor, documented in Literature. They have been shown to provide very similar results and to be in good agreement with experimental data in terms of compressor pressure ratio and rangeability.

The first stage of the compressor was analyzed with both the models in multiple operating conditions, so to characterize the entire range of machine operation, and it was shown to guarantee rangeability in the range 75%–145% of the nominal flow rate. The left limit was, in fact, set a priory and does not exhibit any trace of stall; the right limit is caused by the onset of choking, due to a cavitation process occurring in the
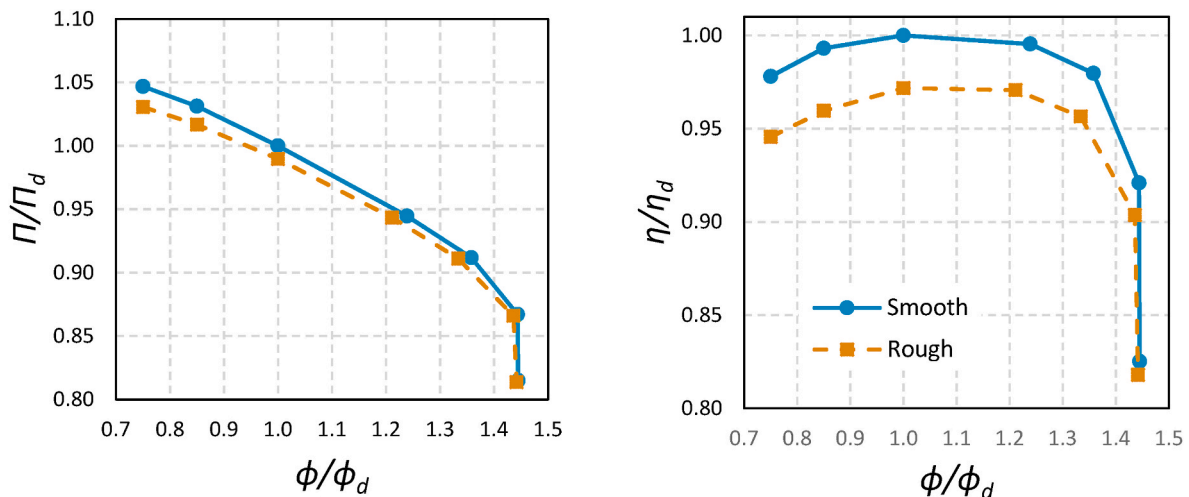

Fig. 14. Effect of the wall roughness on the operational curves of the first stage of the compressor simulated with the HEM. © 2023 Baker Hughes Company - All rights reserved.

intake region of the compressor. A detailed investigation of the compressor aerodynamics has revealed that, thanks to the dedicated machine design of the intake region, two-phase flows are negligible for the left side of the curve, and become significant only above nominal flow rate. The size effect associated with the wall roughness was also investigated, showing a relatively significant influence on the compressor performance (up to 3% of efficiency, for a sand grain roughness of 5 μm), but a negligible impact on the compressor rangeability.

The comparison between the flow predictions obtained with the two solvers has allowed to highlight the differences between the two underlying physical models implemented in them. The predictions obtained with the two models provide nearly identical compressor performance and exhibit only minor differences in local regions of the flow, negligible in terms of fluid kinematics and pressure fields. The main differences appear in the density fields and in the rear part of the channel, in regions of separation and blade wake, where the irreversible entropy generation heats the fluid and, hence, dilates it. Such effect, however, has a negligible impact on the prediction of the compressor right limit, since the cavitation-induced chocking only depends on the flow configuration in the front part of the channel, where the two models provide fully coherent predictions. This finding is also supported by the experimental assessment of the two models, which exhibit full coherence and provides a good matching with the test data.

In light of the results presented in this paper, the HEM in the barotropic formulation appears a relevant tool for the design of sCO$_2$ compressors, also in light of the model simplicity and computational effectiveness. The HEM in complete formulation remains recommended for detailed analyses of the flow, where also thermal effects are relevant. From this perspective, further research is presently ongoing aimed at the development of an eulerian-eulerian multi-phase flow model, with the aim of reproducing in high-fidelity the cavitating flows occurring close to the right limit of the machine.

CRediT authorship contribution statement

Giacomo Persico: Conceptualization, Formal analysis, Funding acquisition, Investigation, Methodology, Project administration, Writing – original draft, Writing – review & editing, Supervision. **Alessandro Romei:** Conceptualization, Data curation, Formal analysis, Investigation, Methodology, Software, Writing – review & editing. **Paolo Gaetani:** Investigation, Writing – review & editing, Conceptualization, Supervision. **Ernani Fulvio Bellobuono:** Conceptualization, Data curation, Validation, Writing – original draft, Writing – review & editing. **Lorenzo Toni:** Conceptualization, Data curation, Supervision, Validation, Writing – review & editing. **Roberto Valente:** Validation, Writing – review & editing, Data curation, Conceptualization.

Declaration of competing interest

The authors declare that they have no known competing financial interests or personal relationships that could have appeared to influence the work reported in this paper.

Data availability

The data that has been used is confidential.

Acknowledgements

Nomenclature

ϕ	flow coefficient
ρ	density [kg/m^3]
η	total-total efficiency
Π	total-total pressure ratio
D	Impeller diameter
M	Mach number
P	Pressure
Q	Volume flow rate [m^3/s]
u	Impeller peripheral speed [m/s]
V	velocity [m/s]
m	streamwise coordinate

Subscripts

0	compressor intake condition
2	impeller outlet condition
d	nominal condition
max	maximum value
merid	meridional component

References

[1] Reimann O. CEWEP energy report III (status 2007-2010). Confederation of European Water-to-Energy Plants 2012. www.cewep.eu.

[2] Marchionni M, Bianchi G, Tassou S. Review of supercritical carbon dioxide (sCO2) technologies for high-grade waste heat to power conversion. SN Appl Sci 2020;2 (611).

[3] Pecnik R, Rinaldi E, Colonna P. Computational fluid dynamics of a radial compressor operating with supercritical CO2. J Eng Gas Turbines Power 2012;134 (12).

[4] Baltadjiev ND, Lettieri C, Spakovszky ZS. An investigation of real gas effects in supercritical CO2 centrifugal compressors. J Turbomach 2015;137.

[5] Pelton R, Allison T, Jung S, Smith N. Design of a wide-range centrifugal compressor stage for supercritical CO2 power cycles. In: ASME Turbo xpo 2017; 2017. Charlotte, NC, USA.

[6] Hacks A, Schuster S, Dohmen HJ, Benra FK, Brillert D. Turbomachine design for supercritical carbon dioxide within the sCO2-HeRo.eu project. J Eng Gas Turbines Power 2018;140.

[7] Marchionni M, Chai L, Bianchi G, Tassou S. Numerical modelling and transient analysis of a printed circuit heat exchanger used as recuperator for supercritical CO2 heat to power conversion systems. Appl Therm Eng 2019;161:114190.

[8] Hosangadi A, Liu Z, Weathers T, Ahuja V, Busby J. Modeling multiphase effects in CO2 compressors at subcritical inlet conditions. J Eng Gas Turbines Power 2019; 141(8).

[9] Persico G, Gaetani P, Romei A, Toni L, Bellobuono E, Valente R. Implications of phase change on the aerodynamics of centrifugal compressors for supercritical carbon dioxide applications. J Eng Gas Turbines Power 2021;143(4).

[10] Dostal V. A supercritical carbon dioxide cycle for next generation. Ph.D. thesis, Massachusetts Institute of Technology; 2004.

[11] Wright SA, Radel RF, Vernon ME, Rochau GE, Pickard PS. Operation and analysis of a supercritical CO2 brayton cycle, sandia report sand2010-0171. 2010.

[12] Alfani D, Binotti M, Macchi E, Silva P, Astolfi M. sCO2 power plants for waste heat recovery: design optimization and part-load operation strategies. Appl Therm Eng 2021;195.

[13] Mortzheim J, Hofer D, Piebe S, McClung A, Moore JJ, Cich S. Challenges with measuring supercritical CO2 compressor perform-ance when approaching the liquid-vapor dome. ASME Turbo Expo 2021;2021.

[14] Toni L, Bellobuono E, Valente R, Romei A, Gaetani P, Persico G. Computational and experimental assessment of a MW-scale supercritical CO2 compressor operating in multiple near-critical conditions. J Eng Gas Turbines Power 2022;144(10).

[15] Bigi M, Bisio V, Evangelisti S, Giancotti M, Milani A, Pellegrini T. Design and operability challenges for supercritical CO2 plants: the sCO2-flex centrifugal compressor test experience. ASME Turbo Expo 2022;2022.

[16] Romei A, Persico G. Computational fluid-dynamic modelling of two-phase compressible flows of carbon dioxide in supercritical conditions. Applied Thermal Engineering; 2021.

[17] Romei A, Gaetani P, Persico G. Computational fluid-dynamic investigation of a centrifugal compressor with inlet guide vanes for supercritical carbon dioxide power systems. Energy; 2022.

[18] Alfani D, Asolfi M, Binotti M, Silva P, Persico G. Part load analysis of a constant inventory supercritical co2 power plant for waste heat recovery in cement industry. In: The 5th European sCO2 conference for energy systems; 2023.

[19] Menter FR. Two-equation eddy-viscosity turbulence models for engineering applications. AIAA J 1994;32(8):1598–605.

[20] Smirnov PE, Menter FR. Sensitization of the SST turbulence model to rotation and curvature by applying the spalart–shur correction term. J Turbomach 2009;131(4): 041010.

[21] Toni L, Bellobuono EF, Valente R, Persico ARPGG. Experimental and numerical performance survey of a MW-scale supercritical CO2 compressor operating in near-critical conditions. In: The 7th international supercritical CO2 power cycle symposium; 2022. San Antonio, Texas.

[22] Brennen CE. Fundamentals of multiphase flows. Cambridge University Press; 2005.

[23] Ringstad K, Allouche Y, Gullo P, Ervik Å, Banasiak K, Hafner A. A detailed review on CO2 two-phase ejector flow modeling. Therm Sci Eng Prog 2020;20:100647.